PERGAMON

International Journal of Heat and Mass Transfer 45 (2002) 4881–4898

International Journal of HEAT and MASS TRANSFER

www.elsevier.com/locate/ijhmt

A fixed-grid finite element based enthalpy formulation for generalized phase change problems: role of superficial mushy region

Madhuchhanda Bhattacharya [1], Tanmay Basak *, K.G. Ayappa

Department of Chemical Engineering, Indian Institute of Science, Bangalore 560 012, India

Received 26 January 2001; received in revised form 28 August 2001

Abstract

The enthalpy method is primarily developed for studying phase change in a multicomponent material, characterized by a continuous liquid volume fraction (ϕ_l) vs temperature (T) relationship. Using the Galerkin finite element method we obtain solutions to the enthalpy formulation for phase change in 1D slabs of pure material, by assuming a superficial phase change region (linear ϕ_l vs T) around the discontinuity at the melting point. Errors between the computed and analytical solutions are evaluated for the fluxes at, and positions of, the freezing front, for different widths of the superficial phase change region and spatial discretizations with linear and quadratic basis functions. For Stefan number (St) varying between 0.1 and 10 the method is relatively insensitive to spatial discretization and widths of the superficial phase change region. Greater sensitivity is observed at $St = 0.01$, where the variation in the enthalpy is large. In general the width of the superficial phase change region should span at least 2–3 Gauss quadrature points for the enthalpy to be computed accurately. The method is applied to study conventional melting of slabs of frozen brine and ice. Regardless of the forms for the ϕ_l vs T relationships, the thawing times were found to scale as the square of the slab thickness. The ability of the method to efficiently capture multiple thawing fronts which may originate at any spatial location within the sample, is illustrated with the microwave thawing of slabs and 2D cylinders.

Keywords: Phase change; Enthalpy formulation; Finite elements; Microwave thawing

1. Introduction

The liquid–solid phase change phenomena is important in many areas of science and engineering, particularly in the metal and food processing industries. For pure materials, phase change occurs at a fixed temperature resulting in an interface which separates distinct solid and liquid phases, e.g. freezing of water or rapid solidification of metals. In contrast, for multicomponent substances, phase change occurs over a temperature range and the solid and liquid phases are separated by a 'mushy' region which is characterized by solids suspended in a liquid region, e.g. solidification of a wax or polymers, thawing of foods etc.

Various numerical methods have been developed to solve phase change problems for pure as well as multicomponent substances. A few earlier studies based on finite element formulations were carried out using the temperature method [1,2]. In the temperature method, strictly applicable for pure substances, the energy balance equation is solved separately for both solid and liquid phases and the moving phase change front is

* Corresponding author. Present address: Department of Chemical Engineering, Indian Institute of Technology, Madras, Chennai 600036, India.

E-mail addresses: mbhattac@bayou.uh.edu (M. Bhattacharya), tbasak@bayou.uh.edu (T. Basak), ayappa@chemeng.iisc.ernet.in (K.G. Ayappa).

[1] Present address: Department of Chemical Engineering, University of Houston, Houston, TX 77204, USA.

0017-9310/02/$ - see front matter
PII: S0017-9310(02)00178-3

Nomenclature

Bi	Biot number
c	velocity of light, $m\,s^{-1}$
C	specific heat capacity, $J\,kg^{-1}\,K^{-1}$
D_s	length scale of a sample, m
E_x	electric field intensity, $V\,m^{-1}$
f	frequency, Hz
h	heat transfer coefficient, $W\,m^{-2}\,K^{-1}$
H	specific enthalpy, $J\,m^{-3}$
I_0	flux of incident radiation, $W\,m^{-2}$
k	thermal conductivity, $W\,m^{-1}\,K^{-1}$
k	propagation constant
k_0	reference thermal conductivity, $W\,m^{-1}\,K^{-1}$
k_{eff}	effective thermal conductivity, $W\,m^{-1}\,K^{-1}$
L	half thickness of slab, m
q	microwave source term, $W\,m^{-3}$
Q	dimensionless microwave source term
R	radius of cylinder, m
St	Stefan number
t	time, s
T	temperature, K
T_I	initial melting point, K
T_M	melting point, K
T_F	final melting point, K
T_∞	ambient temperature, K
T_0	initial temperature, K
T_R	reference temperature, K
u_x	dimensionless electric field
v_x	dimensionless real field component
w_x	dimensionless imaginary field component
z	dimensionless distance
Z	distance, m

Greek symbols

α_0	reference thermal diffusivity, $m^2\,s^{-1}$
γ	dimensionless propagation constant
Γ	front position, m
ϵ_0	free space permittivity, $F\,m^{-1}$
θ	dimensionless temperature
κ'	relative dielectric constant
κ''	relative dielectric loss
λ	latent heat, $J\,kg^{-1}$
ρ	density, $kg\,m^{-3}$
τ	dimensionless time
Φ	basis functions
ϕ_l	liquid volume fraction
ω	angular frequency, $Rad\,s^{-1}$

Subscripts

s	frozen phase
l	liquid phase
L	incidence from left
R	incidence from right

Superscripts

n	newton iterate index
τ	time index

tracked with the appropriate interface conditions. Solutions based on the temperature method, which involve remeshing of the computational domain, become cumbersome for multidimensional problems or in situations where multiple fronts appear e.g. phase change under the influence of microwaves [3]. In contrast, the enthalpy or effective heat capacity method, developed for multicomponent substances, requires a single energy balance equation for the entire domain consisting of co-existing solid, liquid and mushy states. The latent heat is incorporated in the enthalpy for the enthalpy method whereas an effective heat capacity includes the latent heat in the effective heat capacity method. Intermediate states and the phase change region are determined from the equilibrium liquid volume fraction (ϕ_l) vs temperature (T) relationship, thereby avoiding the necessity for a front tracking algorithm. Hence, the method is ideal for studying phase change in multicomponent materials and in situations involving volumetric heat sources where multiple fronts exist.

Due to the simplicity of the effective heat capacity and enthalpy methods, a significant amount of literature [4] has been devoted to extending these methods for pure materials, with the aim of developing a unified formulation for both multicomponent and pure materials. The problem of using these formulations with pure materials is that both the enthalpy and effective heat capacity change rapidly at the melting point due to latent heat evolution. The success of the method then depends on how accurately this information is captured. The Stefan (St) number, which is the ratio of sensible heat to latent heat is a useful indication of the magnitude of the latent heat contribution in a phase change problem. At low (St) numbers, the front movement is slow resulting in steps in the computed temperature [4,5]. Oscillations in the front position and/or temperature occur due to a poor heat balance when the phase change front lies between nodes in a finite difference solution [5,6] or between Gauss quadrature points in a finite element solution [7,8].

A considerable amount of work [9–14] is explicitly devoted to finite element based solutions which seek to improve the performance of the effective heat capacity method. While using the effective heat capacity method

to study phase change in pure materials, the variations primarily revolve around either improving the accuracy of the computed effective heat capacity [9–11] or improving the Jacobian matrix which preserves numerical convergence [12]. A number of proposed effective heat capacity formulations in the literature were compared by Dalhuijsen and Segal [13]. It was found that an explicit-backward time integration with mass lumping of the capacitance matrix yielded the best performance. Numerical studies were carried out for corner freezing of a pure material with $St = 0.4$. Ouyang and Tamma [14] extended this approach [13] to study simultaneous multiple phase change fronts in one-dimensional (1D) pure materials where multiple phase change fronts were obtained by varying boundary conditions. Celentano et al. [12] carried out numerical tests with $St = 0.62$.

In the enthalpy formulation the energy balance equation involves both the enthalpy and temperature, in contrast to the effective heat capacity method which involves only the temperature. When applying the enthalpy method to a pure material, the predicted temperatures at a given point in the domain show a step like behavior [5,6,15,16] and a number of schemes [17–22] have been proposed to remove these oscillations. Voller and Cross [6] estimated the time step iteratively such that the phase change front coincides with any one of the nodes at every time step. Shamsundar [17] simply refined the mesh, thereby minimizing the amount of time the phase change front spends between nodes (which is proportional to the step size observed in the predicted temperatures). Date [18] used a strong enthalpy formulation where an additional constraint of constant temperature was imposed at the phase change front. Caldwell and Chan [20] extended this analysis [18] for cylinders and spherical geometries with $St > 0.1$. Chun and Park [19] recently studied the 1D Stefan problem with a fixed grid finite difference based enthalpy formulation where adaptive time steps were used to restrict the phase change front to within one grid spacing. Comini et al. [21] and McAdie et al. [22] developed finite element based enthalpy formulations where the three level predictor–corrector [21] and regula falsi techniques [22] were implemented to account for the sudden jumps or sharp changes in the enthalpy–temperature relationships. Although these methods do get rid of oscillations, with the exception of the work by Shamsundar [17], they require either temperature constraints or suitable time-integration schemes to keep track of the phase change interface. As a consequence they undermine the inherent advantage of the enthalpy formulation, and are cumbersome to implement in higher dimensions with multiple fronts, or in multicomponent materials that have more than one discontinuity in the ϕ_l vs T relationship. A general and direct method applicable to materials with more complex ϕ_l vs T characteristics including discontinuities is yet to appear in the literature.

The motivation for investigating this problem stems from our interest in studying phase change phenomenon in the presence of microwaves [3], where the effective heat capacity method was successfully used to model phase change in tylose, a food like material characterized by a continuous ϕ_l vs T relationship. Although both the effective heat capacity and enthalpy formulations work well for materials with smooth ϕ_l vs T relationships, we feel that a successful formulation based on the enthalpy method is more attractive than the effective heat capacity method when applied to materials with discontinuous ϕ_l vs T relationships, e.g. ice or brine solution.

In this manuscript we seek to overcome drawbacks in existing enthalpy formulations and arrive at a method that facilitates extension to higher dimensions in a natural manner. In particular the scheme should be robust enough to handle situations with multiple fronts, which arise in applications such as microwave thawing. To this end we analyze the performance of the enthalpy formulation by replacing step like discontinuities that occur in the ϕ_l vs T relationship for pure ice and brine, with a superficial mushy region. We exploit advantages that are inherent in the finite element formulation for improving the accuracy of the energy balance across the interface. This not only involves the use of higher order basis functions, but we also show that higher order Gaussian quadrature schemes at a fixed level of discretization significantly improves accuracy.

We have tested our solution method for solidification of a semi-infinite slab, with Stefan numbers varying between 0.01 and 10. Our numerical solutions are compared with analytical solutions and with other numerical schemes which are prone to oscillations in temperatures and front positions [4]. The case with $St = 0.01$, where the front movement is the slowest, with Dirichlet boundary conditions provides the most severe test to the numerical scheme. To our knowledge numerical tests with $St = 0.01$ have not been reported in the finite element literature. A series of numerical tests with the 1D melting problem is carried out to determine the optimal width of the superficial mushy zone. Sensitivity of the finite element solution is tested by varying the number of elements, type of basis functions and influence of higher order Gauss quadrature schemes. To illustrate the generality of the method we have studied the thawing of finite slabs of ice and 10% brine. The ϕ_l vs T relationship for brine has both the features of a pure and multicomponent material. The ability of the method to capture multiple fronts is illustrated by some representative microwave thawing computations that have been carried out for 1D slabs and 2D cylinders. The microwave thawing computations involve solving the enthalpy equation along with the electric field equations.

2. Theory

2.1. Phase change in 1D slabs

2.1.1. Enthalpy formulation

In the enthalpy formulation the entire domain is governed by a single energy balance equation which accounts for the change of enthalpy within the system. For a general phase change problem, the material may consist of solid, liquid and mushy regions, as shown in Fig. 1. The enthalpy formulation is based on the assumption of local thermal equilibrium between solid and liquid phases and the governing equations are developed by performing microscopic balances on the transport of enthalpy in the solid and liquid fractions within the mushy region [23,24]. Assuming constant density for both solid and liquid phases and absence of any heat source or sink within the system, the energy balance equation based on the enthalpy formulation for a 1D slab is

$$\frac{\partial H}{\partial t} = \frac{\partial}{\partial Z}\left(k_{\text{eff}}\frac{\partial T}{\partial Z}\right), \tag{1}$$

where $k_{\text{eff}} = \phi_l k_l + (1-\phi_l)k_s$ is the effective thermal conductivity with k_l and k_s as liquid and solid phase thermal conductivities respectively. The total enthalpy, $H(T)$, of the system can be written as,

$$H(T) = \rho(1-\phi_l)\int_{T_R}^{T} C_s\,d\alpha + \rho\phi_l\left[\int_{T_R}^{T_l} C_s\,d\alpha + \lambda + \int_{T_l}^{T} C_l\,d\alpha\right], \tag{2}$$

where C_l and C_s are the liquid and solid phase specific heat capacities respectively, λ is the latent heat and ρ is the mean density between the solid and liquid phases. In Eq. (2), T_R represents an arbitrary reference temperature and T_I is the temperature at which phase change initiates. The liquid volume fraction, ϕ_l, which depends on the equilibrium phase diagram for the specific material involved, is a function of temperature at a given position in the sample.

For pure materials, e.g. ice, the liquid volume fraction, ϕ_l, is a step function of temperature with a discontinuity at the melting point T_M, as shown in Fig. 2a. To implement the enthalpy method for these situations, we assume a superficial phase change range of ΔT around T_M, within which ϕ_l is assumed to vary linearly from 0 to 1. This leads to the following functional form for ϕ_l;

$$\phi_l = \begin{cases} 0 & T \leqslant T_I, \\ \dfrac{T-T_I}{(T_F-T_I)} & T_I \leqslant T \leqslant T_F, \\ 1 & T \geqslant T_F \end{cases} \tag{3}$$

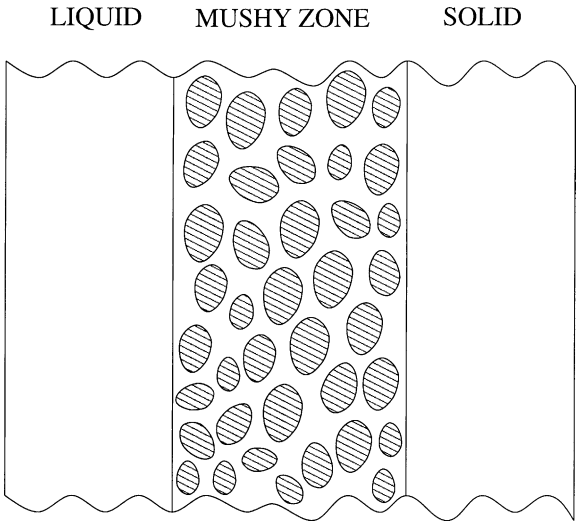

Fig. 1. Schematic of liquid, solid and mushy regions in a slab of multicomponent material undergoing phase change. For a given temperature, the liquid volume fraction, ϕ_l, is determined from the equilibrium ϕ_l vs T relationship for the material.

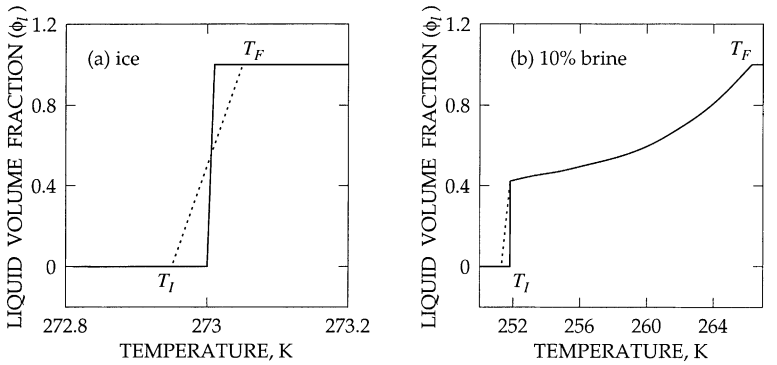

Fig. 2. Liquid volume fraction (ϕ_l) vs temperature (T) profile for (a) ice and (b) 10% brine indicating the superficial phase change region at the point of discontinuity. The ϕ_l vs T data for 10% brine was obtained from the water–NaCl phase diagram [25].

with $T_I = T_M - \Delta T/2$ and $T_F = T_M + \Delta T/2$. With this assumption, $\phi_l(T)$ reduces to a continuous function removing numerical difficulties associated with a step function.

In contrast, $\phi_l(T)$ for 10% brine, which is an aqueous solution of NaCl with a phase change range of T_I to T_F, contains features of both pure as well as multicomponent substance as shown in Fig. 2b. The step jump in ϕ_l from 0 to 0.432 at the initial melting point $T_I = 252$ K is due to a sharp transformation from a solid phase of ice and NaCl to a two phase equilibrium mixture of ice and 23.3% brine. Similar to ice, the discontinuity at $T_I = 252$ K is replaced with a superficial phase change region of width ΔT and within that region, $T_I - \Delta T$ to T_I, the liquid volume fraction is approximated by a linear function. For $T_I \leqslant T \leqslant T_F$, where ϕ_l increases smoothly from 0.432 to 1, the data calculated from the phase diagram for brine using the lever rule [25], shown in Table 1, is fitted by cubic spline using a Matlab routine SPAPI. The functional form of $\phi_l(T)$ for 10% brine used in our calculations is

$$\phi_l = \begin{cases} 0 & T \leqslant T_I - \Delta T, \\ 0.432\frac{(T+\Delta T-T_I)}{\Delta T} & T_I - \Delta T \leqslant T \leqslant T_I, \\ a(j)(T-T_j)^3 + b(j)(T-T_j)^2 + c(j)(T-T_j) + d(j) & T_j \leqslant T \leqslant T_{j+1}, \quad j = 1,\ldots,m-1, \\ 1 & T \geqslant T_F, \end{cases} \tag{4}$$

where $a(j)$, $b(j)$, $c(j)$ and $d(j)$ are the co-efficients of the cubic splines based on m number of data points (Table 1). In Eq. (4), $T_l = T_I = 252$ K and $T_M = T_F = 266.33$ K.

2.1.2. Finite element analysis and solution strategy

In the present study we have analyzed the phase change of a 1D slab of length $2L$ kept at an ambient temperature T_∞ with a uniform initial temperature T_0. Using the dimensionless variables

$$z = \frac{Z}{2L}, \quad \theta = \frac{T - T_\infty}{T_0}, \quad \overline{H} = \frac{H}{\rho_0 C_0 T_0} \quad \text{and} \quad \tau = \frac{\alpha_0 t}{4L^2},$$

the energy balance equation for the slab, Eq. (1), transforms into

$$\frac{\partial \overline{H}}{\partial \tau} = \frac{\partial}{\partial z}\left(\bar{k}_{\text{eff}} \frac{\partial \theta}{\partial z}\right) \tag{5}$$

with

$$\bar{k}_{\text{eff}} = \frac{k_{\text{eff}}}{k_0} \quad \text{and} \quad \alpha_0 = \frac{k_0}{\rho_0 C_0},$$

where α is the thermal diffusivity with suffix '0' representing the reference properties. The initial condition used in our analysis is

$$\theta(\tau = 0) = \frac{T_0 - T_\infty}{T_0} \quad \text{for } 0 \leqslant z \leqslant 1. \tag{6}$$

The Dirichlet boundary conditions, where both ends of the slab are at constant temperatures, are

$$\theta = \frac{T_1 - T_\infty}{T_0} \quad \text{at } z = 0; \quad \text{for } t > 0$$

and

$$\theta = \frac{T_2 - T_\infty}{T_0} \quad \text{at } z = 1; \quad \text{for } t > 0 \tag{7}$$

with T_1 and T_2 as the temperatures at $z = 0$ and 1, respectively. The Neumann boundary conditions, where heat loss occurs by convection from both sides, are

$$\frac{\partial \theta}{\partial z} - Bi\theta = 0 \quad \text{at } z = 0; \quad \text{for } t > 0$$

and

Table 1
The data for liquid volume fraction vs temperature for 10% brine

Temperature (K)	ϕ_l
252	0.0
252	0.432
252.92	0.444
253.73	0.457
254.41	0.465
255.22	0.48
255.97	0.494
256.45	0.508
257.32	0.52
258.0	0.538
258.95	0.56
259.63	0.585
260.51	0.616
261.71	0.673
262.69	0.727
263.42	0.769
264.22	0.82
265.08	0.891
265.94	0.961
266.33	1.0

Data taken from Van Vlack [25].

$$\frac{\partial\theta}{\partial z}+Bi\theta=0 \quad \text{at } z=1; \quad \text{for } t>0 \tag{8}$$

with the dimensionless Biot number, $Bi=((2hL)/k_{\text{eff}})$.

The energy balance equation, Eq. (5), with the appropriate boundary conditions are solved using the Galerkin finite element method to get the temperature profile within the slab. In the Galerkin finite element method the unknown variable θ is expanded in a basis set $\{\Phi\}$;

$$\theta\approx\sum_{k=1}^{N}\theta_k(\tau)\Phi_k(z) \quad \text{for } 0\leqslant z\leqslant 1. \tag{9}$$

The residual equations for Eq. (5), obtained by setting the global error orthogonal to the basis set [26] and using the unconditionally stable finite-difference based Crank–Nicholson method for the time derivative $\partial\overline{H}/\partial\tau$, are

$$R_i=\int_0^1\frac{\overline{H}\left(\theta^{\tau+1}\right)-\overline{H}(\theta^{\tau})}{\Delta\tau}\Phi_i\,\mathrm{d}z+\frac{1}{2}\left[F\left(\theta^{\tau+1},\phi_{\mathrm{l}}^{\tau+1}\right)+F\left(\theta^{\tau},\phi_{\mathrm{l}}^{\tau}\right)\right] \quad i=1,\ldots,N;\ \tau \text{ is the time index,} \tag{10}$$

where the enthalpy from Eq. (2) is,

$$\overline{H}(\theta^{\tau})=(1-\phi_{\mathrm{l}})\frac{\rho C_{\mathrm{s}}}{\rho_0 C_0}\left(\sum_{k=1}^{N}\theta_k^{\tau}\Phi_k-\theta_{\mathrm{R}}\right)+\phi_{\mathrm{l}}\frac{\rho}{\rho_0 C_0}\times\left[C_{\mathrm{s}}(\theta_{\mathrm{I}}-\theta_{\mathrm{R}})+\frac{\lambda}{T_0}+C_{\mathrm{l}}\left(\sum_{k=1}^{N}\theta_k^{\tau}\Phi_k-\theta_{\mathrm{I}}\right)\right] \tag{11}$$

and

$$F(\theta^{\tau},\phi_{\mathrm{l}}^{\tau})=\sum_{k=1}^{N}\phi_k^{\tau}\int_0^1\bar{k}_{\text{eff}}(\phi_{\mathrm{l}}^{\tau})\frac{\mathrm{d}\Phi_i}{\mathrm{d}z}\frac{\mathrm{d}\Phi_k}{\mathrm{d}z}\,\mathrm{d}z+\bar{k}_{\text{eff},1}(\phi_{\mathrm{l}}^{\tau})Bi_1(\phi_{\mathrm{l}}^{\tau})\theta_{\mathrm{l}}^{\tau}\delta_{i1}+\bar{k}_{\text{eff},N}(\phi_{\mathrm{l}}^{\tau})Bi_N(\phi_{\mathrm{l}}^{\tau})\theta_N^{\tau}\delta_{iN}. \tag{12}$$

Although the enthalpy, $\overline{H}(\theta)$, appears as a second unknown in the residual equations, Eq. (10), to be solved along with θ, it can be evaluated at each time step from Eq. (11). Hence the residual equations, Eq. (10), reduce to a set of non-linear equations involving only θ, which are solved at each time step using a Newton–Raphson procedure. The integrals in the residuals are evaluated using 3 point Gaussian quadrature. At each time step the linear $(N\times N)$ system solved for the temperatures $\{\theta^{\tau+1}\}$ is

$$\mathbf{J}\left(\{\theta\}^{n,\tau+1}\right)\left[\{\theta\}^{n,\tau+1}-\{\theta\}^{n+1,\tau+1}\right]=\mathbf{R}\left(\{\theta\}^{n,\tau+1}\right), \tag{13}$$

where n is the Newton iterate index, and $\mathbf{R}(\{\theta\}^{n,\tau+1})$, is the vector of the residuals. The convergence criterion for the Newton iteration based on $\mathbf{R}$ is $(\sum_{i=1}^{N}R_i^2)^{1/2}<10^{-5}$. $\mathbf{J}$ in Eq. (13) is the Jacobian matrix, whose elements are obtained by taking the derivatives of the residual equations, Eq. (10), with respect to the temperature $\{\theta_j^{\tau+1}\}$,

$$J_{i,j}=\frac{1}{\Delta\tau}\int_0^1\frac{\partial\overline{H}\left(\theta^{\tau+1}\right)}{\partial\theta_j^{\tau+1}}\Phi_i\Phi_j\,\mathrm{d}z+\frac{1}{2}\left[\frac{\partial F\left(\theta^{\tau+1},\phi_{\mathrm{l}}^{\tau+1}\right)}{\partial\theta_j^{\tau+1}}\right]. \tag{14}$$

The solutions are obtained for both quadratic and linear basis functions. At a particular time, the position of the phase change front, $\Gamma(\tau)$, is calculated by first locating the element which contains the melting point, T_{M}. The exact position of the phase change front, $z=\Gamma(\tau)$, is then determined by interpolating with the basis functions using the finite element expansion,

$$T_{\mathrm{M}}=\sum_{k=1}^{N}T_k\Phi_k(z). \tag{15}$$

2.2. Modeling: microwave thawing

In this section, we have analyzed thawing of 1D slabs and 2D cylinders in the presence of volumetric heat sources due to microwave propagation within the samples. Microwaves are assumed to be incident normally on the opposite faces of the slab as shown in Fig. 3a and on an infinite cylinder as shown in Fig. 3b. The incident microwave is a uniform plane wave, with the electric and magnetic components varying in intensity only in the direction of wave propagation (z axis). The enthalpy formulation due to microwave heating, for a domain consisting of solid, liquid and mushy regions is governed by a single energy balance equation

$$\frac{\partial H}{\partial t}=\nabla\cdot k_{\text{eff}}\nabla T+q(T) \tag{16}$$

with $q(T)$ as the absorbed microwave power. The wave propagation due to electric field, E_x, is governed by [27,28]

$$\nabla^2E_x+k^2(\phi_{\mathrm{l}})E_x=0, \tag{17}$$

where E_x varies in the y–z plane only and $k=(\omega/c)(\kappa'(\phi_{\mathrm{l}})+\mathrm{i}\kappa''(\phi_{\mathrm{l}}))^{1/2}$, the spatially varying propagation constant, depends on $\kappa'(\phi_{\mathrm{l}})$ the relative dielectric constant and $\kappa''(\phi_{\mathrm{l}})$, the relative dielectric loss. Here $\omega=2\pi f$, where f is the frequency of the electromagnetic wave and c is the velocity of light. We assume that the dielectric properties are temperature dependent only due to their dependence on ϕ_{l} in the mushy region. Hence in regions of pure liquid and solid the dielectric properties are assumed to be independent of temperature. The dielectric properties in the superficial mushy region follow the mixture rules as discussed in our earlier work [3].

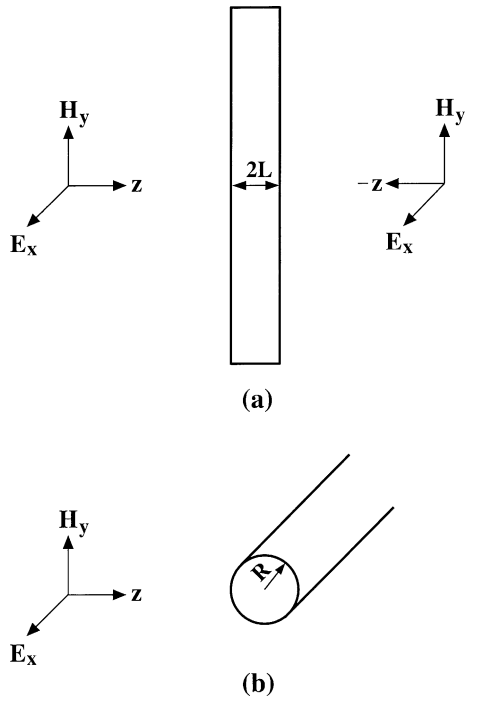

Fig. 3. Schematic of (a) 1D slab and (b) 2D cylinder exposed to plane electromagnetic waves.

The absorbed power per unit volume is

$$q = \tfrac{1}{2}\omega\epsilon_0\kappa'' E_x E_x^*, \tag{18}$$

where ϵ_0 is the free space permittivity and E_x^* is the complex conjugate of E_x. For a given flux of incident radiation, I_0, in free space, the incident electric field intensity, E_0, is given by,

$$E_0 = \sqrt{\frac{2I_0}{c\epsilon_0}}. \tag{19}$$

Using the dimensionless variables,

$$u_x = \frac{E_x}{E_0} \quad \text{and} \quad \nabla^* = D_s\nabla,$$

Eq. (17) reduces to

$$\nabla^{*2}(u_x) + \gamma^2(\phi_1)u_x = 0, \tag{20}$$

where u_x is the electric field intensity, $\gamma(\phi_1) = ((D_s\omega)/c)(\kappa'(\phi_1) + i\kappa''(\phi_1))^{1/2}$ is the propagation constant and $D_s = 2L$ for slabs, $D_s = R$ for 2D cylinders. Substituting the complex field variable $u_x = v_x + iw_x$ into Eq. (20) and equating the real and imaginary components, we get

$$\nabla^{*2}v_x + \chi_1(\phi_1)v_x - \chi_2(\phi_1)w_x = 0 \tag{21}$$

and

$$\nabla^{*2}w_x + \chi_2(\phi_1)v_x + \chi_1(\phi_1)w_x = 0 \tag{22}$$

with $\chi_1(\phi_1) = ((D_s^2\omega^2)/c^2)\kappa'(\phi_1)$ and $\chi_2(\phi_1) = ((D_s^2\omega^2)/c^2)\kappa''(\phi_1)$.

For uniform plane waves incident on a sample some of the radiation is scattered and the rest is absorbed. For 1D slab, boundary conditions [27] for the real and imaginary components are,

$$\left.\begin{aligned} \frac{dv_x}{dz} - \frac{2\omega L}{c}w_x &= \frac{4\omega L}{c}\sin\left(\frac{\omega L}{c}\right) \\ \frac{dw_x}{dz} + \frac{2\omega L}{c}v_x &= \frac{4\omega L}{c}\cos\left(\frac{\omega L}{c}\right) \end{aligned}\right\} \quad \text{at } z = 0 \tag{23}$$

and

$$\left.\begin{aligned} \frac{dv_x}{dz} + \frac{2\omega L}{c}w_x &= -\frac{E_R}{E_L}\frac{4\omega L}{c}\sin\left(\frac{\omega L}{c}\right) \\ \frac{dw_x}{dz} - \frac{2\omega L}{c}v_x &= -\frac{E_R}{E_L}\frac{4\omega L}{c}\cos\left(\frac{\omega L}{c}\right) \end{aligned}\right\} \quad \text{at } z = 1. \tag{24}$$

Radiation boundary conditions [28] used at the outer surface of the cylinder are

$$\begin{aligned} \boldsymbol{n}\cdot\nabla^* v_x = {} & \sum_{n=0}^{\infty}\mathrm{Re}(C_n)\cos n\phi + \sum_{n=0}^{\infty}\mathrm{Re}(D_n) \\ & \times \int_0^{2\pi} v_x(1,\phi')\cos n(\phi-\phi')\,d\phi' \\ & - \sum_{n=0}^{\infty}\mathrm{Im}(D_n)\int_0^{2\pi} w_x(1,\phi')\cos n(\phi-\phi')\,d\phi' \end{aligned} \tag{25}$$

and

$$\begin{aligned} \boldsymbol{n}\cdot\nabla^* w_x = {} & \sum_{n=0}^{\infty}\mathrm{Im}(C_n)\cos n\phi + \sum_{n=0}^{\infty}\mathrm{Im}(D_n) \\ & \times \int_0^{2\pi} v_x(1,\phi')\cos n(\phi-\phi')\,d\phi' \\ & + \sum_{n=0}^{\infty}\mathrm{Re}(D_n)\int_0^{2\pi} w_x(1,\phi')\cos n(\phi-\phi')\,d\phi' \end{aligned} \tag{26}$$

with the coefficients

$$C_n = \frac{\epsilon_n i^n \omega R}{c}\left[J_n'\left(\frac{\omega R}{c}\right) - J_n\left(\frac{\omega R}{c}\right)\frac{H_n^{(1)'}\left(\frac{\omega R}{c}\right)}{H_n^{(1)}\left(\frac{\omega R}{c}\right)}\right] \tag{27}$$

and

$$D_n = \frac{\omega R\delta_n H_n^{(1)'}\left(\frac{\omega R}{c}\right)}{c\pi H_n^{(1)}\left(\frac{\omega R}{c}\right)} \tag{28}$$

and

$$\epsilon_n = \begin{cases} 1, & n = 0; \\ 2, & \text{otherwise}, \end{cases} \quad \text{and} \quad \delta_n = \begin{cases} 1/2, & n = 0; \\ 1, & \text{otherwise}. \end{cases} \tag{29}$$

In Eqs. (27) and (28), J_n and $H_n^{(1)}$ are the Bessel and Hankel functions of the first kind respectively and prime indicates the first derivatives.

Dimensionless form of the energy balance equation in presence of microwave, Eq. (16), is

$$\frac{\partial \overline{H}}{\partial \tau} = \nabla^* \left(\bar{k}_{\text{eff}} \nabla^* \theta \right) + Q(\theta), \tag{30}$$

where the expression for the microwave power term in Eq. (30) is,

$$Q(\phi_1(\theta)) = \frac{D_s^2 \omega \epsilon_0 \kappa''(\phi_1) E_0^2}{2 k_0 T_0} (v_x^2 + w_x^2). \tag{31}$$

The initial condition used in the analysis is

$$\theta(\tau = 0) = \frac{T_0 - T_\infty}{T_0}, \quad \text{for } -1 \leqslant y, z \leqslant 1. \tag{32}$$

In the analysis, Neumann convective boundary condition is used which can be expressed as

$$-\mathbf{n} \cdot \bar{k}_{\text{eff}} \nabla^* \theta = Bi\theta. \tag{33}$$

The coupled energy balance and the electric field equations with the appropriate boundary conditions are solved using Galerkin finite element method in the similar manner as discussed in Section 2.1.2. The details of the solution procedure for microwave thawing in 1D slabs and 2D cylinders are given in [3,29].

3. Numerical tests

3.1. Solidification of a semi-infinite slab

To evaluate the performance of the finite element solution of the enthalpy method we have analyzed the freezing of a semi-infinite slab of pure material with melting point $T_M = 273$ K. We consider a 50 cm slab with the solution computed within the first 5 cm. Our simulations are carried out using the ϕ_l vs T in Eq. (3) with a superficial phase change range of $\Delta T = 0.1$ K. The slab is initially at a uniform temperature $T_0 = 274$ K. At time $t = 0$ the surface of the slab at $z = 0$ is lowered to temperature $T_l = 272$ K and maintained at that temperature for the entire solidification process. Using three node quadratic elements with $\Delta Z = 0.1$ cm and a time step $\Delta t = 0.002$ s, the front positions and the temperature history at $Z = 0.4$ cm are predicted and compared with the analytical solutions [30] and the numerical results from a finite volume method [4] used with a step function representation for ϕ_l vs T. We have assumed constant material properties, $k_s = k_l = 4.2 \times 10^2$ W m^{-1} K^{-1}, $\rho = 1000$ kg m^{-3} and $C_s = C_l = 4.2 \times 10^3$ J kg^{-1} K^{-1}, similar to those used by Voller [4]. Our direct method requires only 3–4 Newton iterations in each time step whereas a modified effective heat capacity method typically requires 7–8 iterations [12].

Fig. 4 compares the predicted temperature history and the front positions with analytical solutions and previously reported finite volume based results [4] for three different St numbers ($St = C_s(T_M - T_l)/\lambda$), 0.1, 1 and 10 corresponding to the latent heat values of $\lambda = 4.2 \times 10^4$, 4.2×10^3 and 4.2×10^2 J kg^{-1} respectively. At $St = 0.1$, the front movement is relatively slow ($\Gamma(t)$ (cm) $= 0.378\sqrt{t}$) due to the large ratio of latent heat to sensible heat, allowing the element undergoing phase change to remain at the melting point for a longer time. During this time, nodes away from the freezing region reach a pseudo steady state giving rise to steps in the temperature as observed in the finite volume based [4] results (Fig. 4a). The width of the steps have been shown to be equal to the time taken for the element undergoing phase change to freeze [5]. This situation is characteristic of the problems associated with previous finite difference solutions of the enthalpy formulation [15,24]. At $St = 10$, latent heat effects are small compared to the sensible heat removing oscillations in the temperature due to rapid front movement ($\Gamma(t)$ (cm) $= 0.926\sqrt{t}$). However poor resolution of the front position results in steps in the reported numerical results [4] for the front positions at $St = 10$. In contrast, our results are free of oscillations in both temperature and front positions for all the cases considered here. We have also tested our method with 50 linear elements ($\Delta Z = 0.1$ cm). The results (not shown here) indicate that at $St = 10$ and 1, both front positions and temperatures agree well with the analytical solutions, but small oscillations are observed at $St = 0.1$, which disappear on increasing the number of elements.

The success of the enthalpy formulation hinges on the accuracy of the computed enthalpy whose variation across the phase change region increases with decreasing St number (see insets in Fig. 7). In a finite element formulation this entails computing integrals involving the enthalpy over the element containing the phase change front (Eq. (10)). Latent heat contributions will be accurately captured if the domain of the superficial phase change region is over a sufficient number of Gauss points. This suggests that for a given discretization and width of the superficial phase change range, the accuracy of the computed enthalpy can also be improved by using a higher order Gauss quadrature. These effects in relation to errors in the flux and front position for $0.01 \leqslant St \leqslant 10$ and different spatial discretizations are analyzed in the next section.

3.2. Errors in flux and front positions

In order to study the performance of our solution strategy we have computed solutions for the solidification problem discussed above, at St numbers 10, 1, 0.1 and 0.01 and computed the errors associated with the predicted front position and heat flux at the interface for 7 and 27 quadratic elements. Among the four St numbers, $St = 0.01$ represents the most severe case with an

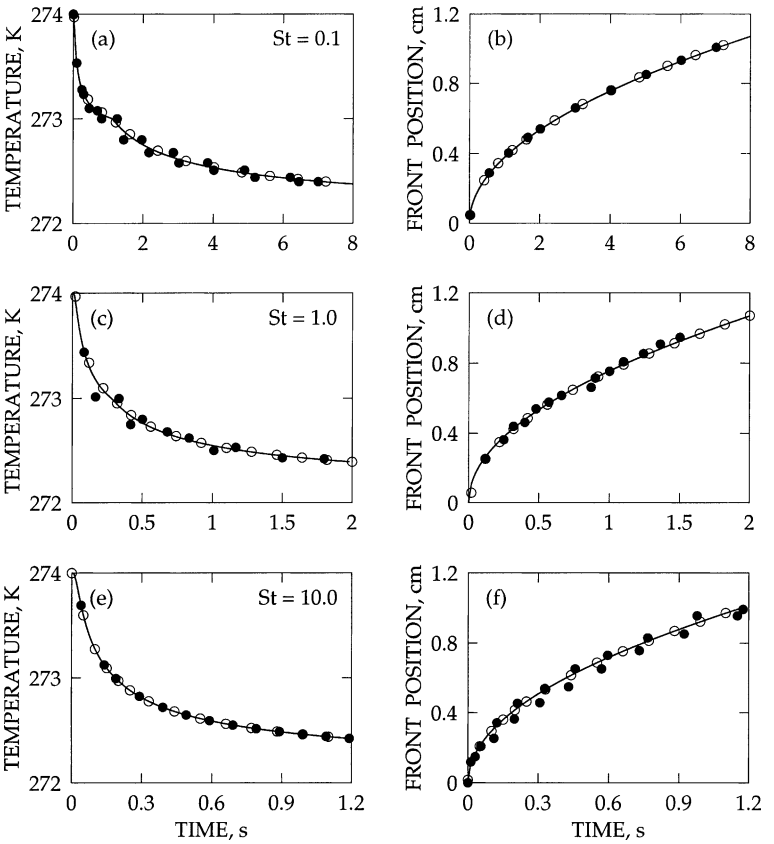

Fig. 4. Temperatures at $Z = 0.4$ cm and front positions, for (a) and (b) $St = 0.1$, (c) and (d) $St = 1.0$ and (e) and (f) $St = 10$, (—) analytical solution, (●) finite volume based solution [4]. (○) Finite element solution with 50 quadratic elements. In all cases the width of the superficial phase change region was $\Delta T = 0.1$ K.

enthalpy variation of about 420×10^6 J m^{-3} across the superficial phase change region, in comparison to a variation of 0.42×10^6 J m^{-3} at $St = 10$. The enthalpy was obtained using Eq. (2) with $T_R = 272$ K, ambient temperature. Note that, the maximum variation in total enthalpy, H, within the mushy region is $\rho\lambda$. We define the error in the heat flux at the phase change interface as

$$E_{\text{flux}} = \frac{J_{\text{anal}} - J_{\text{num}}}{J_{\text{anal}}}, \tag{34}$$

where

$$J_{\text{anal}} = \rho\lambda \frac{\mathrm{d}\Gamma(t)}{\mathrm{d}t} \tag{35}$$

is obtained from the analytical expression for, $\mathrm{d}\Gamma(t)/\mathrm{d}t$ [30] and J_{num} is calculated by numerically evaluating the velocity of the front using the computed values of the front positions at two successive time steps;

$$J_{\text{num}} = \rho\lambda \frac{\Gamma(t+\Delta t)_{\text{num}} - \Gamma(t)_{\text{num}}}{\Delta t}. \tag{36}$$

The error in the front position is calculated as,

$$E_{\text{front}} = \frac{\Gamma(t)_{\text{anal}} - \Gamma(t)_{\text{num}}}{\Gamma(t)_{\text{anal}}}. \tag{37}$$

At $St = 10$, 1 and 0.1, the problems are solved with an initial guess of uniform temperature, T_0 and a superficial phase change range of $\Delta T = 0.1$ K. In order to obtain a good initial guess for the Newton–Raphson method at $St = 0.01$, we have used the temperature profile obtained from the analytical solution at time $t = 0.001$ s as the initial guess, with $\Delta T = 0.06$ K. In all cases $0.0001 \leqslant \Delta t \leqslant 0.009$ s is used as the first time step and $\Delta t = 0.002$ s is used for subsequent steps.

Fig. 5 illustrates the predicted front positions and temperatures at $Z = 1$ and 3 cm for $St = 10$ and 0.01 with 7 ($\Delta Z = 0.625$ cm) and 27 ($\Delta Z = 0.18$ cm) quadratic elements. The associated errors, E_{flux} and E_{front}, are illustrated in Fig. 6. At $St = 10$, both front positions and temperatures are in very good agreement with the analytical solutions. The corresponding errors, E_{flux} and

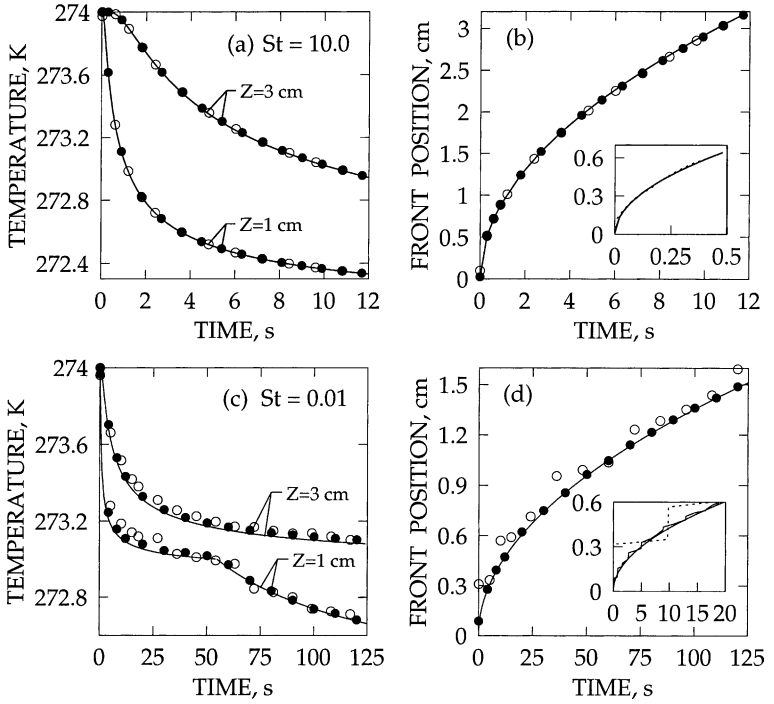

Fig. 5. Temperatures at $Z = 1$ and 3 cm and front positions for (a) and (b) $St = 10$, $\Delta T = 0.1$ K and (c) and (d) $St = 0.01$, $\Delta T = 0.06$ K. (—) Analytical solution, (●) finite element solution, 27 quadratic elements ($\Delta Z = 0.18$ cm), (○) finite element solution, 7 quadratic elements ($\Delta Z = 0.625$ cm). The insets show the front positions during the initial stages.

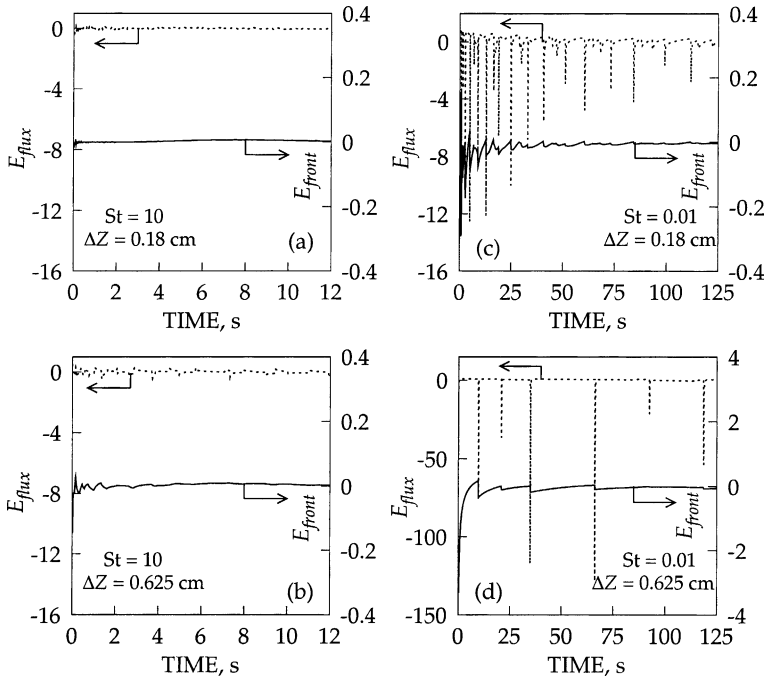

Fig. 6. Errors E_{flux} and E_{front} with time for $St = 10$ and 0.01 with 27 and 7 quadratic elements.

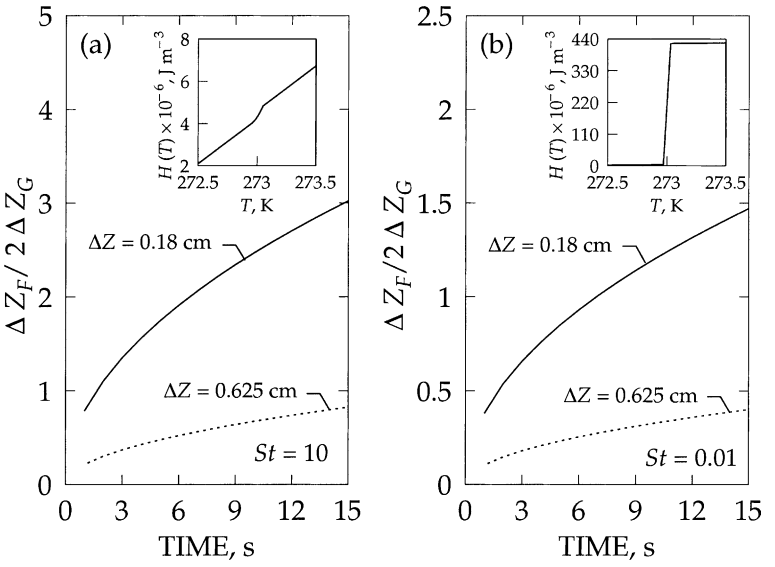

Fig. 7. Variation of $\Delta Z_F/2\Delta Z_G$ ratio with time for $St = 10$ and 0.01 with 27 and 7 quadratic elements. ΔZ_F, the spatial width of the freezing range increases with time.

E_{front}, are almost zero for the entire solidification process, indicating that the enthalpy is being evaluated accurately. At $St = 0.01$, due to the larger variation in enthalpy across the superficial phase change region (see inset of Fig. 7), inaccuracies in the computed enthalpy are greatly magnified. This results in greater errors both in the flux and front positions (see inset in Fig. 5) with an order of magnitude increase in the errors for $\Delta Z = 0.625$ cm compared to $\Delta Z = 0.18$ cm, where the temperatures and front positions are in reasonably good agreement with the analytical solutions. Note that, the definition of E_{flux} (Eq. (34)) involves numerically evaluated velocities of finite element based front. The error in velocities of front is greatly magnified due to error in numerical front position ($\Gamma(t)$). Hence in some cases, E_{flux} is around ±130 whereas E_{front} is ±0.3. However, with a very few exceptions, E_{flux} and E_{front} are within a tolerance limit.

For a given superficial freezing range, the accuracy of the computed enthalpy will depend on the ratio of the spatial width of the freezing range (ΔZ_F) to the distance between two successive Gauss quadrature points (ΔZ_G) in the element. A minimum value of $\Delta Z_F/\Delta Z_G = 1$ will allow the phase change region to span over at least 2 Gauss points ensuring a more accurate evaluation of the enthalpy and energy balance at the interface. We have calculated the width of the freezing range ΔZ_F from the analytical solutions [30] by assuming that T_F lies in the liquid region and T_I lies in the solid region. The ratio of $\Delta Z_F/2\Delta Z_G$ for same widths of the freezing interval as used in the calculations for Figs. 5 and 6 are shown in Fig. 7 along with the enthalpy variations across the superficial phase change region. In all cases it is observed that ΔZ_F is smallest during the initial stages of thawing and is seen to increase with time (more rapidly for larger St numbers). At a fixed discretization, this increase in ΔZ_F is reflected in a decrease in the magnitude of the errors in the flux and front positions as seen in Fig. 6c and d.

At $St = 10$ and $\Delta Z = 0.18$ cm, $\Delta Z_F/2\Delta Z_G > 1$ during the entire time (Fig. 7a) reflecting the low errors at this discretization, whereas for $\Delta Z = 0.625$ cm, the ratio is below 1 (Fig. 7a) for the first 15 s leading to the higher errors at the initial period of solidification. In contrast, for $St = 0.01$, $\Delta Z_F/2\Delta Z_G < 1$ for first 5–10 s with $\Delta Z = 0.18$ cm and $\Delta Z_F/2\Delta Z_G < 0.5$ for first 15 s with $\Delta Z = 0.625$ cm (Fig. 7b). The lower values of $\Delta Z_F/2\Delta Z_G$ and the sharp variations of the enthalpy (inset Fig. 7b) across the superficial phase change region leads to greater errors in the flux and front positions at $St = 0.01$.

3.3. Effect of superficial mushy region

The assumption of a superficial phase change region in our method, removes the steps in temperatures and front positions, yielding oscillation free solutions which are in excellent agreement with the analytical solutions over the entire range of St numbers (Figs. 4 and 5). Provided the width of the superficial phase change region is sufficiently small our method is able to eliminate the problem of pseudo-steady states that lead to step formation and compute the temperature of the real system very accurately. We find that for $0.1 \leqslant St \leqslant 10$ the accuracy of the computed front positions and the

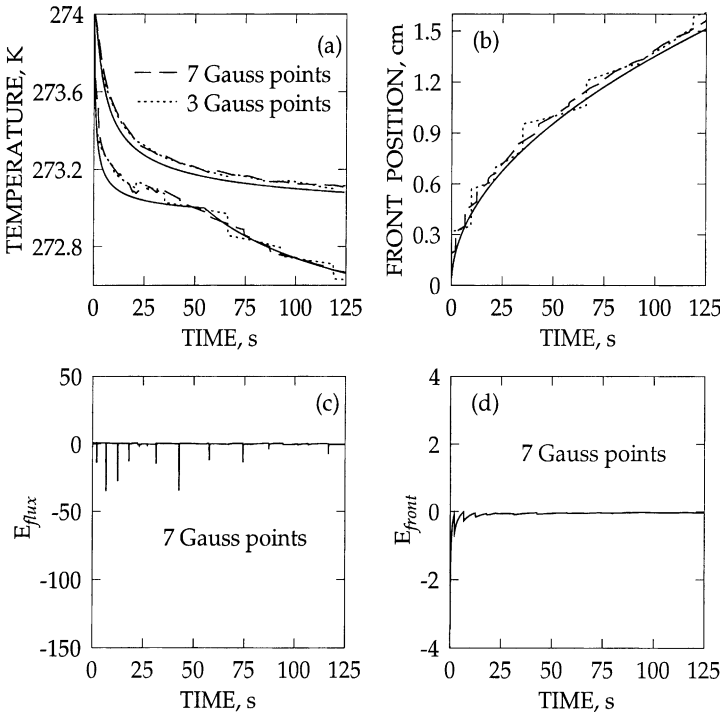

Fig. 8. Effect of increasing Gauss quadrature points from 3 to 7 while computing the integrals in the residual for a coarse mesh of seven elements. Compare the errors with those reported for 3 Gauss points in Fig. 6.

temperatures are relatively insensitive for widths of the superficial phase change region, $0.02 \leqslant \Delta T \leqslant 0.1$. We also find that greater thickness of mushy region, $0.1 \leqslant \Delta T \leqslant 0.5$ may be used for higher values of T_1 at $z = 0$. However, we recommend that, optimally $\Delta T = 0.1$ K may be used irrespective of T_1. At $St = 0.01$, due to the sharp variation of the enthalpy across the superficial phase change range compared to the other St numbers the solutions are sensitive to the widths of the superficial phase change region, $0.02 \leqslant \Delta T \leqslant 0.1$. At $St = 0.01$, optimal results were obtained at $\Delta T = 0.06$ for 27 quadratic elements (Fig. 5c and d).

3.4. Effect of Gauss points

The accuracy of the computed enthalpy may be improved by increasing $\Delta Z_F/\Delta Z_G$ ratio via increasing the number of Gauss integration points. To illustrate the effect of increasing Gauss quadrature points on the solution, we have analyzed the case for $St = 0.01$ with a coarse mesh of 10 elements ($\Delta Z = 0.625$ cm) for 3 and 7 Gauss integration points. Fig. 8 compares the predicted temperatures at $Z = 1$ and 3 cm and the front positions. The errors, E_{flux} and E_{front} are shown for 7 Gauss points in Fig. 8c and d, (errors with 3 Gauss points are shown in Fig. 6). The large steps in the front positions and temperatures are substantially reduced by increasing the Gauss points from 3 to 7. This clearly illustrates the need to accurately evaluate the enthalpy to preserve the energy balance in the system. Note that although the accuracy of the computed enthalpy can be improved by increasing the number of Gauss points, the accuracy of the final solution is limited by the discretization error for this coarse mesh.

4. Thawing of 1D finite slab

4.1. Thawing of ice and 10% brine slabs

We have applied our solution method to study the thawing of finite slabs of ice and 10% brine with Dirichlet boundary conditions. The Dirichlet boundary conditions offer the most severe test to a numerical scheme for phase change of pure materials, due to the sharp gradient in temperatures during the initial stages of thawing [7]. A uniform initial temperature of 260 K for ice and 245 K for 10% brine is used. In all cases the surface of the slab is held at 300 K, corresponding to $St = 0.18$ for ice. The material properties for ice and 10% brine used are given in Table 2. We assume that the latent heat of 10% brine is similar to that of ice. The simulations are carried out for slab thicknesses varying between 1 and 5 cm. A superficial mushy region of

Table 2
The material properties used for the analysis of phase change in a finite slab of water, tylose and 10% brine in the solid (s) and the liquid (l) phases

Property	water_s	water_l	tylose_s	tylose_l	10% brine_s	10%brine_l
Heat capacity C ($\text{J kg}^{-1}\,\text{K}^{-1}$)	2051	4226	2090	3520	2051	3360
Thermal conductivity k ($\text{W m}^{-1}\,\text{K}^{-1}$)	2.22	0.56	1.3	0.5	2.22	0.56
Density, ρ (kg m^{-3})	917	999	961	1057	–	1060
Latent heat, λ (J kg^{-1})	3.34×10^5		2.34×10^5		3.34×10^5	

$\Delta T = 0.1$ K was used for ice and brine. For each of the cases, we have used 50 quadratic elements and the time steps range between 0.001 and 0.1 s. A linear temperature profile within a thin layer at $t = 0$ was assumed as an initial guess for ice and brine. Fig. 9 illustrates the thawing of a 1 cm slab of ice and Fig. 10 illustrates the thawing for a 1 cm slab of 10% brine. The step-like behavior of the liquid volume fraction and the sharp transition in the temperature at the melting point indicate that the method is able to accurately capture the features for melting of a pure substance. For 10% brine (Fig. 10) the slab consists of a mushy region for $0.4 \leqslant \phi_l \leqslant 1.0$ and the method is able to efficiently handle the discontinuity in the liquid volume fraction. We have also analyzed the problem with heat loss from both ends (Neumann boundary condition). It is observed that for this case converged solutions are obtained for a large time step of 10 s and the method works well for uniform initial temperatures.

4.2. Thawing time vs slab thickness

The correlation between thawing time, t_{th}, with the slab thickness, $2L$, for different materials are shown in Fig. 11. The total thawing time of a slab subjected to Dirichlet boundary conditions at both ends increases

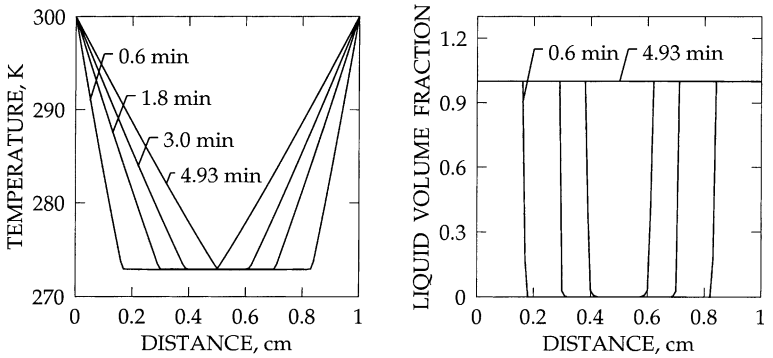

Fig. 9. Temperature and liquid volume fraction (ϕ_l) distributions for a 1 cm ice slab with both ends at 300 K (Dirichlet boundary conditions). The sharp ice water interface is realistically captured with a superficial phase change region of width $\Delta T = 0.1$ K.

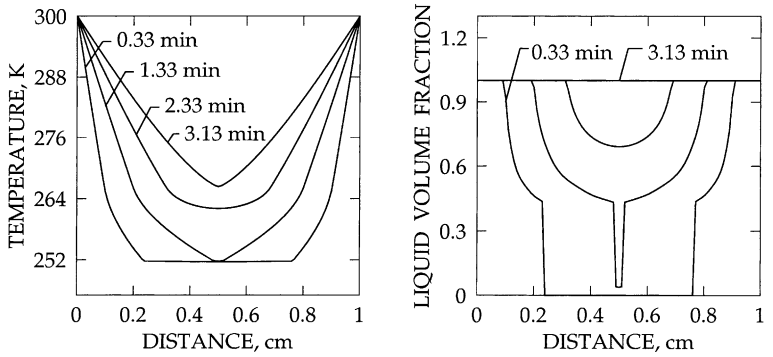

Fig. 10. Temperature and liquid volume fraction (ϕ_l) distributions for a 1 cm 10% brine slab with both ends at 300 K (Dirichlet boundary conditions).

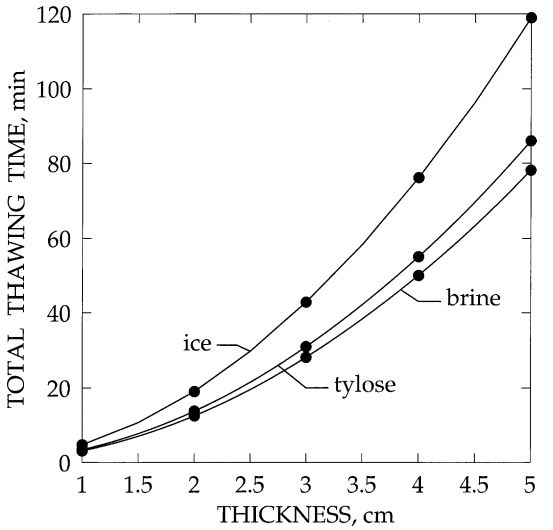

Fig. 11. Power law relationship between thawing time and slab thickness for ice, tylose and 10% brine.

monotonically with the sample thickness following a power law relationship, $t_{th} \propto (2L)^n$. The exponent, $n = 2$, is a classical result for the Stefan problem for thawing of a pure substance where melting occurs at a distinct temperature. Our numerical results show that a power law with $n = 2$ behavior is also observed for materials like 10% brine and tylose [3] which melt over a temperature range.

5. Microwave thawing of 1D slab

The enthalpy formulation has been applied to study microwave thawing in order to investigate the propagation of thawing fronts which may appear/initiate at any place within a sample. We have carried out simulations for ice which offers the most severe case as discussed in the earlier sections. A uniform initial temperature, $T_0 = 270$ K with slab thicknesses 0.5 and 2 cm are used for the simulation. In all cases an ambient temperature, $T_\infty = 300$ K and a heat transfer coefficient, $h = 2\ \mathrm{W\,m^{-2}\,K^{-1}}$ are used. The dielectric properties of ice and water are obtained from Basak and Ayappa [3]. For each case, we have used 50 quadratic elements and the time steps range between 0.005 and 0.05 s. A superficial mushy region of $\Delta T = 0.1$ K is used. The results for microwave heating in a single phase are compared with Ayappa et al. [27] and the results were in excellent agreement. During microwave thawing the definition of Stefan number (St) may not be used. However, based on a maximum temperature of 280 K during thawing, an estimate of modified Stefan number, $St_{\mathrm{m}} = 0.14$, may be obtained. At the initial stages of thawing, St_{m} is very low and it is greater in later stages of thawing. For all stages of thawing, our direct method is seen to efficiently capture the thawing fronts.

Fig. 12 illustrates the power, temperature and liquid volume fraction profiles at various times for the 0.5 cm slab, exposed to microwaves of intensity $3\ \mathrm{W\,cm^{-2}}$ from both sides. At the initial stages of thawing, due to

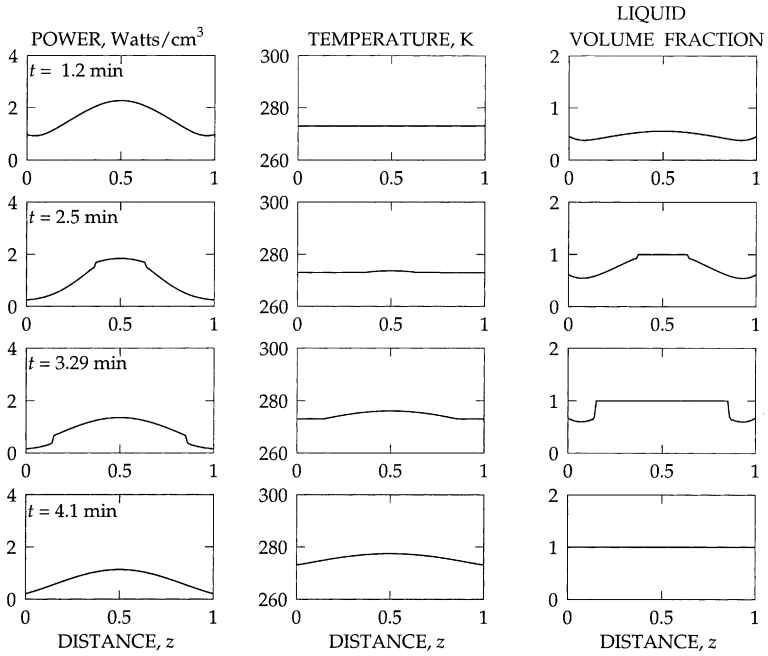

Fig. 12. Power, temperature and liquid volume fraction profiles during microwave thawing of a 0.5 cm ice slab exposed to microwaves. $f = 2450$ MHz, $I_{\mathrm{OL}} \equiv I_{\mathrm{OR}} = 3\ \mathrm{W\,cm^{-2}}$.

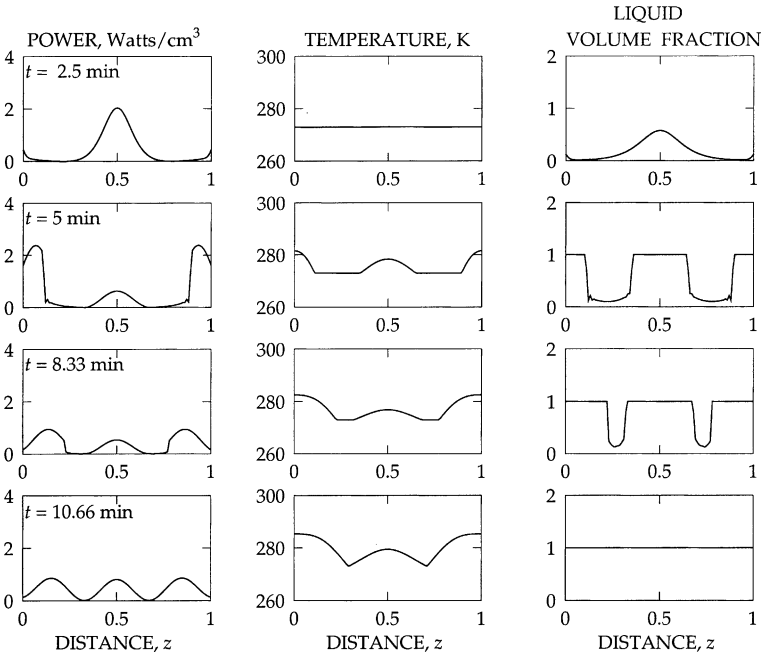

Fig. 13. Power, temperature and liquid volume fraction profiles during microwave thawing of a 2 cm ice slab exposed to microwaves. $f = 2450$ MHz, $I_{OL} \equiv I_{OR} = 3\ \mathrm{W\,cm^{-2}}$.

constructive interference by the standing waves, a peak in absorbed power is observed at the center. Consequently, at 2.5 min, liquid starts forming at the center resulting in a sharp phase change front at the center. At the later stage of thawing, the phase change front expands from the center towards the faces of the slab. Results for thawing of 2 cm slab are shown in Fig. 13. At the initial stages, although maxima in absorbed power is observed at the center, maxima is shifted at the outer faces of the slab during the later stages. Consequently, multiple liquid regions are formed at the center and outer faces. In all the cases, our method is able to capture the step like behavior in the liquid volume fraction at the melting point. The enthalpy formulation requires no additional conditions at the phase change front and is particularly suited to capture multiple phase change fronts in the presence of volumetric heat sources.

6. Microwave thawing of 2D cylinder

In this section, the method is applied to study microwave thawing in 2D cylinders. We have used 10×10 bi-quadratic elements in the upper-half of r–θ domain [29] with a time step ranges between 0.02 and 0.05 s. We have tested the enthalpy formulation in the absence of microwaves for 2D cylinders, with a superficial mushy region of $\Delta T = 0.1$ K and boundary conditions $T = 283$ K [29]. Microwave heating in a single phase is validated with Ayappa et al. [28]. In all these cases, the test results were in good agreement.

We have carried out simulation studies for ice cylinders with a uniform initial temperature, $T_0 = 265$ K. In all cases an ambient temperature, $T_\infty = 300$ K and a heat transfer coefficient, $h = 2\ \mathrm{W\,m^{-2}\,K^{-1}}$ are used. Fig. 14 illustrates the power, temperature and liquid volume fraction contours at various times for 0.5 cm cylinder exposed to microwaves of intensity $1\ \mathrm{W\,cm^{-2}}$. At the initial stages, due to constructive interference produced by the standing waves set up in the cylinder, a peak in power absorption occurs near the side not exposed to microwaves. Consequently, liquid (indicated by shaded region) starts forming at the unexposed side and the liquid region is preceded by a superficial mushy region/solid region. The sample temperature at the unexposed side is 330 K, whereas the temperature at the exposed side is 273 K when the sample is almost thawed. Results for thawing of a 2 cm radius cylinder are shown in Fig. 15. At 10 and 25 min, it is observed that thawing occurs simultaneously at various places within the cylinder. Due to power peaks in the exposed, center and unexposed sides, multiple thawing fronts are observed. These situations illustrate the ability of the method to capture the presence of multiple fronts with complex shapes that may arise during thawing.

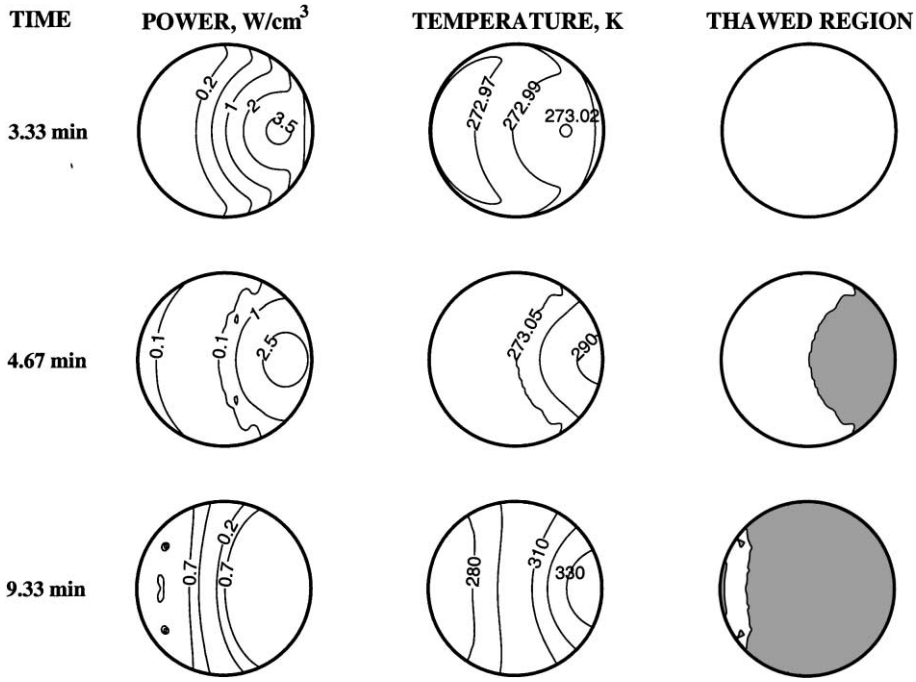

Fig. 14. Power, temperature and liquid volume fraction profiles during microwave thawing of a 0.5 cm ice cylinder exposed to microwaves. The shaded region represents the liquid. $f = 2450$ MHz, $I_0 = 1$ W cm^{-2}.

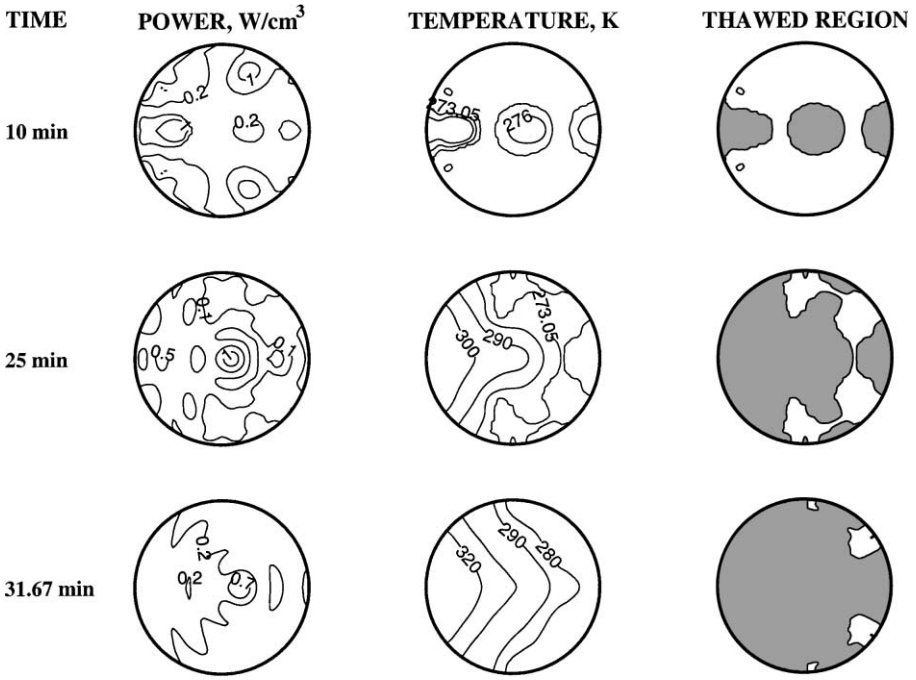

Fig. 15. Power, temperature and liquid volume fraction profiles during microwave thawing of a 2 cm ice cylinder exposed to microwaves. The shaded region represents the liquid. $f = 2450$ MHz, $I_0 = 1$ W cm^{-2}.

7. Conclusion

Using Galerkin finite element method we have solved the 1D phase change problems for both pure and multicomponent substances using the enthalpy method. The single energy balance equation, consisting of both enthalpy and temperature, is solved for the entire domain and the state of the material is determined from the equilibrium ϕ_l vs T relationships. For materials like ice and 10% brine which have discontinuities in the $\phi_l(T)$ curves, a superficial phase change region is assumed around the point of discontinuity.

Various numerical tests were carried out to establish the optimal numerical strategy for $0.01 \leqslant St \leqslant 10$. The solutions obtained for a pure material with a superficial phase change region are free of oscillations for $0.01 \leqslant St \leqslant 10$ and temperatures and front positions are in excellent agreement with analytical solutions. The accuracy in temperature and front positions are insensitive for widths of superficial phase change region with the exception of $St = 0.01$ where optimal results were obtained at $\Delta T = 0.06$ for 27 quadratic elements. Our study indicates that the enthalpy can be computed accurately if the superficial freezing range spans at least 3 Gauss quadrature points while using quadratic elements. For the same reasons an increase in the number of Gauss points at a fixed discretization also improves the accuracy of the computed solution. In perspective, the accuracy of numerical solutions of the phase change problems depends on mesh size, number of Gauss quadrature points and width of the superficial mushy region. Note that, the problem of missing the phase change interface is most severe in a 1D situation.

We feel that our method is general, and can conveniently be used for materials with more complex phase diagrams that result in ϕ_l vs T curves with more than one point of discontinuity. With the introduction of the superficial phase change region, the method does not require keeping track of the phase change region. This is particularly advantageous while solving problems in higher dimensions and melting with internal heat generation where interface locations and shapes are not known a priori. In contrast to previous methods proposed in the literature, the enthalpy formulation proposed here is based on fixed mesh and is easy to implement. We have applied the method for melting of finite slabs of ice and 10% brine. In all cases the sharp interface corresponding to a pure material is accurately captured. Total thawing time for finite slabs are seen to scale as $(2L)^2$. The microwave thawing examples in 1- and 2D illustrate that the method efficiently captures multiple thawing fronts without any significant reformulation of the procedure. Since the basic problem implementation does not depend on the geometry considered, extension to multidimensional cases is relatively straightforward. We have recently applied the enthalpy formulation to investigate the microwave thawing of 2D cylinders in the presence of internal convective effects [31].

References

[1] B. Rubinsky, E.G. Cravahlo, A finite element method for the solution of one-dimensional phase change problems, Int. J. Heat Mass Transfer 24 (1981) 1987–1989.
[2] J. Yoo, B. Rubinsky, Numerical computation using finite elements for the moving interface in heat transfer problems with phase transformation, Numer. Heat Transfer 6 (1983) 209–222.
[3] T. Basak, K.G. Ayappa, Analysis of microwave thawing of slabs with the effective heat capacity method, Am. Inst. Chem. Eng. J. 43 (7) (1997) 1662–1674.
[4] V.R. Voller, An overview of numerical methods for solving phase change problems, Adv. Numer. Heat Transfer 1 (1996).
[5] G. Bell, On the performance of the enthalpy method, Int. J. Heat Mass Transfer 25 (1982) 587–589.
[6] V.R. Voller, M. Cross, Accurate solutions of moving boundary problems using the enthalpy method, Int. J. Heat Mass Transfer 24 (1981) 545–556.
[7] J.A. Dantzig, Modelling liquid–solid phase changes with melt convection, Int. J. Numer. Meth. Eng. 28 (1989) 1769–1785.
[8] K. Morgan, R.W. Lewis, O.C. Zienkiewicz, An improved algorithm for heat conduction problems with phase change, Int. J. Numer. Meth. Eng. 12 (1978) 1191–1195.
[9] S. Del Giudice, G. Comini, R.W. Lewis, Finite element simulation of freezing processes in soils, Int. J. Numer. Anal. Meth. Geomech. 2 (1978) 223–235.
[10] E.G. Lemmon, Phase change techniques for finite element conduction codes, in: R.W. Lewis, K. Morgan (Eds.), Numerical Methods in Thermal Problems (Proceedings Conference), Swansea, Pineridge Press, Swansea, 1979, pp. 149–158.
[11] Q.T. Pham, The use of lumped capacitance in the finite-element solution of heat conduction problems with phase change, Int. J. Heat Mass Transfer 29 (1986) 285–291.
[12] D. Celentano, E. Onate, S. Oller, A temperature-based formulation for finite element analysis of generalized phase-change problems, Int. J. Numer. Meth. Eng. 37 (1994) 3441–3465.
[13] A.J. Dalhuijsen, A. Segal, Comparison of finite element techniques for solidification problems, Int. J. Numer. Meth. Eng. 23 (1986) 1807–1829.
[14] T. Ouyang, K.K. Tamma, Finite element simulations involving simultaneous multiple interface fronts in phase change problems, Int. J. Heat Mass Transfer 39 (8) (1996) 1711–1718.
[15] L.E. Goodrich, Efficient numerical technique for one-dimensional thermal problems with phase change, Int. J. Heat Mass Transfer 21 (1978) 615–621.
[16] V.R. Voller, M. Cross, P.G. Walton, Assessment of weak solution techniques for solving Stefan problems, in: R.W. Lewis, K. Morgan (Eds.), Numerical Methods in Thermal

Problems, Pineridge Press, Swansea, UK, 1979, pp. 172–181.
[17] N. Shamsundar, Comparison of numerical methods for diffusion problems with moving boundaries, in: D.G. Wilson, A.D. Soloman, P.T. Boggs (Eds.), Moving Boundary Problems, Academic Press, New York, 1978, pp. 165–185.
[18] A.W. Date, A strong enthalpy formulation for the Stefan problem, Int. J. Heat Mass Transfer 34 (1991) 2231–2235.
[19] C.K. Chun, S.O. Park, A fixed-grid finite difference method for phase change problems, Numer. Heat Transfer, Part B 38 (2000) 59–73.
[20] J. Caldwell, C.C. Chan, Numerical solutions of the Stefan problem by the enthalpy method and the heat balance integral method, Numer. Heat Transfer, Part B 33 (1998) 99–117.
[21] G. Comini, S. Del Giudice, O. Saro, A conservative algorithm for multidimensional conduction phase change, Inter. J. Numer. Meth. Eng. 30 (1990) 697–709.
[22] R.L. McAdie, J.T. Cross, R.W. Lewis, D.T. Gethin, A finite element enthalpy technique for solving coupled nonlinear heat conduction/mass diffusion problems with phase change, Int. J. Numer. Meth. Heat Fluid Flow 5 (1995) 907–921.
[23] N. Shamsundar, E.M. Sparrow, Analysis of multidimensional conduction phase change via the enthalpy model, ASME—J. Heat Transfer 97 (1975) 333–342.
[24] V.R. Voller, C.R. Swaminathan, B.G. Thomas, Fixed grid techniques for phase change problems: A review, Int. J. Numer. Meth. Eng. 30 (1990) 875–898.
[25] L.H. Van Vlack, in: Elements of Materials Science, Addison-Weseley Publishing Company, Reading, MA, 1960, p. 300.
[26] J.T. Oden, J.N. Reddy, An Introduction to the Mathematical Theory of Finite Elements, John Wiley and Sons, New York, 1976.
[27] K.G. Ayappa, H.T. Davis, E.A. Davis, J. Gordon, Analysis of microwave heating of materials with temperature-dependent properties, Am. Inst. Chem. Eng. J. 37 (1991) 313–322.
[28] K.G. Ayappa, H.T. Davis, E.A. Davis, J. Gordon, Two-dimensional finite element analysis of microwave heating, Am. Inst. Chem. Eng. J. 38 (1992) 1577–1592.
[29] T. Basak, Analysis of microwave thawing, Ph.D. Thesis, Indian Institute of Science, Bangalore, India, 1999.
[30] H.S. Carslaw, J.C. Jaeger, Conduction of Heat in Solids, Clarendon Press, Oxford, 1959.
[31] T. Basak, K.G. Ayappa, Influence of internal convection during microwave thawing of cylinders, Am. Inst. Chem. Eng. J. 47 (2001) 835–850.